Paneth cells as a site of origin for intestinal inflammation

Published in final edited form as:
Nature. 2013 November 14; 503(7475): . doi:10.1038/nature12599.

Paneth cells as a site of origin for intestinal inflammation

Timon E. Adolph[1,*], **Michal F. Tomczak**[2,*], **Lukas Niederreiter**[1,*], **Hyun-Jeong Ko**[2,16,*], **Janne Böck**[3], **Eduardo Martinez-Naves**[4], **Jonathan N. Glickman**[5], **Markus Tschurtschenthaler**[1,6], **John Hartwig**[7], **Shuhei Hosomi**[2], **Magdalena B. Flak**[2], **Jennifer L. Cusick**[2], **Kenji Kohno**[8], **Takao Iwawaki**[9,10], **Susanne Billmann-Born**[3], **Tim Raine**[1], **Richta Bharti**[3], **Ralph Lucius**[11], **Mi-Na Kweon**[12], **Stefan J. Marciniak**[13], **Augustine Choi**[14], **Susan J. Hagen**[15], **Stefan Schreiber**[3], **Philip Rosenstiel**[3], **Arthur Kaser**[1,17,#], and **Richard S. Blumberg**[2,#]

[1]Division of Gastroenterology and Hepatology, Department of Medicine, University of Cambridge, Cambridge CB2 0QQ, United Kingdom

[2]Division of Gastroenterology, Department of Medicine, Brigham and Women's Hospital, Harvard Medical School, 75 Francis Street, Boston, MA 02115 USA

[3]Institute for Clinical Molecular Biology, Christian-Albrechts-Universität zu Kiel, D-24105 Kiel, Germany

[4]Department of Microbiology and Immunology, Facultad de Medicina, Universidad Complutense de Madrid, Madrid, Spain

[5]GI Pathology Division, Miraca Life Sciences, Newton, MA 02464, USA

[6]Department of Medicine II (Gastroenterology & Hepatology), Medical University Innsbruck, A-6020 Innsbruck, Austria

[7]Translational Medicine Division, Department of Medicine, Brigham and Women's Hospital, Harvard Medical School,75 Francis Street, Boston, MA 02115 USA

[8]Department of Cell Biology, Graduate School of Biological Sciences, Nara Institute of Science and Technology NAIST, 8916 5 Takayama, Ikoma, Nara, Japan

[9]Advanced Scientific Research Leaders Development Unit, Gunma University 3-39-22 Showa-machi, Maebashi, Gunma 371-8511, Japan

[10]Iwawaki Initiative Research Unit, Advanced Science Institute, RIKEN, 2-1 Hirosawa, Wako, Saitama 351-0198, Japan

[11]Anatomical Institute, Christian-Albrechts-Universität zu Kiel, D-24098 Kiel, Germany

Correspondence and requests for materials should be addressed to R.S.B. or A.K. (rblumberg@partners.org or ak729@cam.ac.uk).
[16]Current address: Laboratory of Microbiology and Immunology, College of Pharmacy, Kangwon National University, Chuncheon 200-701, South Korea
[17]Previous address: Department of Medicine II (Gastroenterology & Hepatology), Medical University Innsbruck, A-6020 Innsbruck, Austria
[*]These authors contributed equally to this work.
[#]These authors contributed equally to this work.

Author Contributions T.E.A., M.F.T., L.N. and H.-J.K. performed most experiments, together with J.B., E.M.N., M.T., S.H., M.B.F., S.B.-B., T.R., R.B. and M.N.K. J.L.C. helped preparing the manuscript. S.J.H. and J.H. contributed electron microscopic analysis, A.C. provided expertise in autophagy assessment, and R.L. in histology of Paneth cells. S.S. and P.R. designed, generated and analyzed an essential mouse strain. K.K., T.I. and S.J.M. provided an essential mouse strain. J.N.G. assessed intestinal inflammation. A.K. und R.S.B. devised and coordinated the project, and together with T.E.A. and M.F.T. wrote the manuscript and designed the experiments.

The authors declare no competing financial interests.

Supplementary Information is linked to the online version of the paper at www.nature.com/nature.

[12]Mucosal Immunology Section, Laboratory Science Division, International Vaccine Institute, Seoul 151-818, Korea

[13]Department of Medicine, University of Cambridge, Cambridge Institute for Medical Research (CIMR), Wellcome Trust/MRC Building, Hills Road, Cambridge, CB2 0XY, United Kingdom

[14]Division of Pulmonary and Critical Care Medicine, Department of Medicine, Brigham and Women's Hospital, Harvard Medical School, 75 Francis Street, Boston, MA 02115 USA

[15]Department of Surgery, Beth Israel Deaconess Medical Center, Boston, MA 02215 USA

Abstract

Autophagy related 16-like 1 (*ATG16L1*) as a genetic risk factor has exposed the critical role of autophagy in Crohn's disease (CD)[1]. Homozygosity for the highly prevalent *ATG16L1* risk allele, or murine hypomorphic (HM) activity causes Paneth cell dysfunction[2,3]. As *Atg16l1*^{HM} mice do not develop spontaneous intestinal inflammation, the mechanism(s) by which ATG16L1 contributes to disease remains obscure. Deletion of the unfolded protein response (UPR) transcription factor X-box binding protein-1 (*Xbp1*) in intestinal epithelial cells (IECs), whose human orthologue harbors rare inflammatory bowel disease (IBD) risk variants, results in endoplasmic reticulum (ER) stress, Paneth cell impairment and spontaneous enteritis[4]. Unresolved ER stress is a common feature of IBD epithelium[4,5], and several genetic risk factors of CD affect Paneth cells[2,4,6-9]. Here we show that impairment in either UPR (*Xbp1*$^{\Delta IEC}$) or autophagy function (*Atg16l1*$^{\Delta IEC}$ or *Atg7*$^{\Delta IEC}$) in IECs results in each other's compensatory engagement, and severe spontaneous CD-like transmural ileitis if both mechanisms are compromised. *Xbp1*$^{\Delta IEC}$ mice exhibit autophagosome formation in hypomorphic Paneth cells, which is linked to ER stress via protein kinase RNA-like endoplasmic reticulum kinase (PERK), elongation initiation factor 2α (eIF2α) and activating transcription factor 4 (ATF4). Ileitis is dependent on commensal microbiota and derives from increased IEC death, inositol requiring enzyme 1α (IRE1α)-regulated NFκB activation and tumor necrosis factor signaling which are synergistically increased when autophagy is deficient. ATG16L1 restrains IRE1α activity and augmentation of autophagy in IECs ameliorates ER stress-induced intestinal inflammation and eases NFκB overactivation and IEC death. ER stress, autophagy induction and spontaneous ileitis emerge from Paneth cell-specific deletion of *Xbp1*. Genetically and environmentally controlled UPR function within Paneth cells may therefore set the threshold for the development of intestinal inflammation upon hypomorphic ATG16L1 function and implicate ileal CD as a specific disorder of Paneth cells.

The UPR and autophagy are integrally linked pathways[10]. To investigate their relationship in the intestinal epithelium, we stably transduced the small IEC line MODE-K with a short hairpin *Xbp1* (sh*Xbp1*) lentiviral vector (Extended Data Fig. 1a)[4]. We observed increased levels of ATG7, Beclin1 (Extended Data Fig. 1b) and phosphatidylethanolamine (PE)-conjugated microtubule-associated protein 1 light chain 3 β (LC3-II) relative to LC3-I compared to control-silenced (*shCtrl*) cells (Extended Data Fig. 1c). Increased autophagic flux accounted for this given increased levels of LC3-II relative to LC3-I observed after inhibition of autophagosome-lysosome fusion by bafilomycin[11] (Extended Data Fig. 1d). Increased GFP-LC3 punctae were seen in *shXbp1* compared to *shCtrl* MODE-K cells transfected with a green fluorescent protein (GFP)-LC3-expressing vector[12] (Extended Data Fig. 1e, f), and increased numbers of autophagic vacuoles in *shXbp1* compared to *shCtrl* cells (Extended Data Fig.1g, h). Accordingly, isolated primary IECs from the small intestine of Villin (V)-*Cre*$^{+}$*;Xbp1*$^{fl/fl}$ ('*Xbp1*$^{\Delta IEC}$')[4] mice backcrossed onto C57BL/6 (B6) exhibited nearly complete consumption of LC3-I and a relative increase in LC3-II (Fig. 1a and Extended Data Fig.1i), stable amounts of ATG7 presumably reflecting a combination of increased production and consumption, elevated levels of ATG16L1 and Beclin1 (Fig. 1b and Extended Data Fig. 1j) and autophagosomes and degradative autophagic vacuoles

consistent with autophagy induction in hypomorphic[4] Paneth cells, and to a lesser extent goblet cells (data not shown), compared to *V-Cre*$^{-}$*;Xbp1*$^{fl/fl}$ (*Wt*) mice (Fig. 1c and Extended Data Fig. 1k). To gain temporal control of *Xbp1* deletion and ability to monitor autophagy *in situ* and exclude the role of chronic inflammation[4] in this induction, we generated V-*CreER*^{T2}*;Xbp1*$^{fl/fl}$ (‘*Xbp1*$^{T\text{-}\Delta IEC}$’) mice on a B6 background crossed to *GFP-LC3* transgenic mice[12]. Three days after tamoxifen-induced *Xbp1* deletion (Extended Data Fig.2a), although mature Paneth cells remained present with little detectable inflammation (data not shown), punctate GFP signal accumulation was greatest at the bottom of the crypts of Lieberkühn (Fig. 1d, e), and co-localized with lysozyme-positive Paneth cells (Extended Data Fig. 2b). Purified crypts of *Xbp1*$^{T\text{-}\Delta IEC}$ mice revealed increased LC3-I/II conversion and reduced p62 compared to *Wt* mice (Extended Data Fig.2c). Thus, *Xbp1* loss in IECs induced autophagy most notably in Paneth cells.

Although *Xbp1*-deficient IECs exhibited broad evidence of ER stress[4] (Extended Data Fig. 2d-j), an examination of *shXbp1*, relative to *shCtrl*, MODE-K cells demonstrated a particularly significant increase in phosphorylated (p)-PERK and its substrate p-eIF2α (Fig. 1f) with the latter reversed by *Perk*-silencing identifying it as the factor responsible for p-eIF2α formation (Extended Data Fig. 3a). Increased p-eIF2α was also detected in primary IECs of *Xbp1*$^{\Delta IEC}$ (Fig. 1g and Extended Data Fig. 3b) and *Xbp1*$^{T\text{-}\Delta IEC}$ mice (Extended Data Fig. 3c). Consistent with PERK-eIF2α involvement in autophagy induction, ATF4, a transcriptional effector of this pathway, and its transcriptional target, C/EBP-homologous protein (CHOP; encoded by *Ddit3*), were increased in primary IECs of *Xbp1*$^{\Delta IEC}$ mice (Fig. 1g and Extended Data Fig. 3b), and chromatin-immunoprecipitation (ChIP) with anti-ATF4 demonstrated increased binding to the *Map1lc3b* (*LC3b*) (Fig. 1h) and *Atg7* (Fig. 1i) promoters, both of which contain ATF4 binding sites[13], in *shXbp1* relative to *shCtrl* MODE-K cells. ATG7 is essential for the formation of the ATG12-ATG5 conjugate during autophagy[10,14]. *shXbp1* MODE-K cells exhibited increased *LC3b* and *Atg7* expression compared to *shCtrl* MODE-K cells (Extended Data Fig. 3d), and *Perk* co-silencing abrogated ATG7 induction observed in *shXbp1* compared to *shCtrl* MODE-K cells (Extended Data Fig. 3a). Salubrinal, a selective inhibitor of eIF2α dephosphorylation[15] (Extended Data Fig.2a), increased the accumulation of GFP-LC3 punctae primarily in Paneth cells, in both *Xbp1*-sufficient and –deficient IECs (Fig. 1j and Extended Data Fig. 2b and 3e), and provoked increased levels of LC3-II relative to LC3-I (Extended Data Fig. 3f) and CHOP (Extended Data Fig. 3f) in *Xbp1*$^{T\text{-}\Delta IEC}$ mice, along with, importantly, an amelioration of the acute enteritis (Fig. 1k and Extended Data Fig. 3g). Similarly, silencing of growth arrest and DNA damage-inducible protein 34 (*Gadd34*; encoded by *Ppp1r15a*), part of the protein phosphatase 1 complex that dephosphorylates eIF2α[16], led to increased eIF2α phosphorylation and ATG7 expression in *shXbp1* compared to *shCtrl* MODE-K cells (Extended Data Fig. 3h, i). *Xbp1*$^{\Delta IEC}$*;Gadd34*$^{+/-}$ mice with hypomorphic GADD34 function exhibited increased p-eIF2α and ATG7 in purified crypt epithelial cells compared to *Xbp1*$^{\Delta IEC}$*;Gadd34*$^{+/+}$ mice (Extended Data Fig. 3j). Thus, PERK-p-eIF2α is a critical mediator of UPR-induced autophagy primarily in Paneth cells consequent to XBP1-deficiency.

These studies let us hypothesize that autophagy may function as a compensatory mechanism in IECs upon sustained ER stress. We therefore generated *V-Cre*$^{+}$*;Atg7*$^{fl/fl}$*;Xbp1*$^{fl/fl}$ (‘*Atg7/Xbp1*$^{\Delta IEC}$’) mice[14]. IECs from *Atg7*$^{\Delta IEC}$ mice lacked LC3-II formation and the ATG5-ATG12;ATG16L1 complex (Extended Data Fig. 4a). *Atg7/Xbp1*$^{\Delta IEC}$ mice demonstrated a complete absence of UPR-induced autophagy (Fig. 2a and Extended Data Fig. 4a-c), and a remarkable worsening of ileitis compared to *Xbp1*$^{\Delta IEC}$ mice. In notable contrast to *Xbp1*$^{\Delta IEC}$ mice, where inflammation was limited to the mucosa, >70% of *Atg7/Xbp1*$^{\Delta IEC}$ mice developed discontinuous submucosal or transmural inflammation, characterized by acute and chronic inflammation extending in an abrupt knife-like fashion to muscularis propria

and serosa, closely resembling the early fissuring ulcerations and fistulous tracts observed in human CD (Fig. 2b, c and Extended Data Fig. 4d). In contrast to *Xbp1*$^{\Delta IEC}$ mice, enteritis in *Atg7/Xbp1*$^{\Delta IEC}$ mice progressed over the 18 week observation period such that at this time point all animals exhibited submucosal or transmural disease (Extended Data Fig. 4e, f).

ATG16L1 is a major genetic risk factor for CD[1,17], especially ileal CD[18]. Complex formation of ATG16L1 protein with ATG12-ATG5 defines the site of LC3 PE conjugation during autophagosome formation[19,20]. ATG16L1 protein expression was markedly increased in *Xbp1*$^{\Delta IEC}$ compared to *Wt* primary IECs (Fig. 1b and Extended Data Fig. 1j), presumably consequent to PERK/eIF2α/ATF4-dependent transactivation of *Atg7* and *LC3b* promoters and stabilization by the ATG7-induced ATG12-ATG5 complex[21]. We therefore developed mice with a floxed *Atg16l1* allele that would allow for IEC-specific deletion via V-*Cre* ('*Atg16l1*$^{\Delta IEC}$'; Extended Data Fig. 4g-i). Paneth cells in *Atg16l1*$^{\Delta IEC}$ mice demonstrated a reduction in their overall size and number of granules, similar to gene-trap-targeted *Atg16l1*^{HM} mice[2,3] (Extended Data Fig. 4j-n). IECs from *Atg16l1*$^{\Delta IEC}$, compared to *Wt* mice, exhibited reduced expression of ATG7 and the ATG12-ATG5 conjugate (Extended Data Fig. 5a), along with disruption of the secretory pathway with a distended ER, reduced size and number of secretory granules, a loss of homeostatic autophagy (Fig. 2d and Extended Data Fig.5b, c) and increased p62 immunoreactivity in crypts (Extended Data Fig. 5d). To address the role of ATG16L1 under ER stress conditions, we generated V-*Cre*$^{+}$;*Atg16l1*$^{fl/fl}$;*Xbp1*$^{fl/fl}$ ('*Atg16l1/Xbp1*$^{\Delta IEC}$') mice. *Atg16l1/Xbp1*$^{\Delta IEC}$ mice, which lacked UPR-induced autophagy (Extended Data Fig. 5b, c), developed severe spontaneous ileitis compared to *Xbp1*$^{\Delta IEC}$ or *Atg16l1*$^{\Delta IEC}$ mice, with discontinuous submucosal or transmural inflammation in >70% of 18-week old animals (Fig. 2b, e and Extended Data Fig. 5e, f) with features similar to those observed in *Atg7/Xbp1*$^{\Delta IEC}$ mice, and present in two distinct animal facilities (Fig. 2b, e and Extended Data Fig. 5g). This phenotype highlights the important compensatory role played by autophagy and in particular ATG16L1 in defending against inflammation arising from unabated ER stress precisely in the small intestinal epithelium as a consequence of XBP1-deficiency.

ATG7 hypofunction in hepatocytes can induce ER stress[22], raising the possibility that cross-talk between the UPR and autophagy may be bi-directional in IECs. Isolated *Atg16l1*$^{\Delta IEC}$ crypts exhibited increased *Xbp1* splicing compared to *Wt* (Fig. 2f, g) and increased *grp78* expression (Extended Data Fig. 5h) localized to the crypt bottom (Fig. 2h). Dextran sodium sulfate, a colitis model involving ER stress in IECs that can be treated with ER stress-relieving chaperones[23,24], induced more inflammation in *Atg16l1*$^{\Delta IEC}$ compared to *Wt* mice (Extended Data Fig. 5i-l), similar to *Atg16l1*^{HM} mice[3]. Thus, disturbances in autophagy within IECs also affect the UPR, and autophagy-associated factors such as ATG16L1 endow IECs with the ability to mitigate ER stressors that are commonplace at the mucosal surface[25].

We next turned our attention to mechanisms by which autophagy counteracts ER stress and synergistic increase in intestinal inflammation when absent. Increased numbers of terminal deoxynucleotidyl transferase dUTP nick end labeling (TUNEL)$^{+}$ cells in *Atg16l1/Xbp1*$^{\Delta IEC}$ and *Atg7/Xbp1*$^{\Delta IEC}$ mice (Extended Data Fig. 6a, b) correlated with enteritis severity in double-mutant, in contrast to *Xbp1*$^{\Delta IEC}$ mice (Extended Data Fig. 6b), and, as demonstrated for *Atg16l1/Xbp1*$^{\Delta IEC}$ mice, concomitantly with increasing age (Extended Data Fig. 6c and Video 1). Silencing of *Atg16l1* in *shXbp1* MODE-K cells significantly increased the proportion of apoptotic cells *in vitro* (Fig. 3a and Extended Data Fig. 6d), indicating that increased apoptosis could function as an initial event in intestinal inflammation. Further, IEC-associated NFκB activation, a critical player in intestinal inflammation[26], was absent in primary IECs from *Wt* mice and gradually increased in *Atg16l1*$^{\Delta IEC}$, *Xbp1*$^{\Delta IEC}$, and *Atg16l1/Xbp1*$^{\Delta IEC}$ mice (Fig. 3b and Extended Data Fig. 6e, f). *shXbp1* MODE-K cells exhibited

increased NFκB activation when stimulated with tumor necrosis factor (TNF) (Fig. 3c and Extended Data Fig. 6g, h) or Toll-like receptor ligands (data not shown) relative to *shCtrl* MODE-K cells, demonstrating increased sensitivity of XBP1-deficient IECs to inflammatory and environmental stimuli. Inhibition of NFκB by treatment with BAY11-7082 decreased IEC death in $Xbp1^{T\text{-}\Delta IEC}$ mice (Fig. 3d and Extended Data Fig. 6i) and protected from enteritis in both $Xbp1^{T\text{-}\Delta IEC}$ and $Xbp1^{\Delta IEC}$ mice (Fig. 3e and Extended Data Fig. 6j) relative to vehicle treated mice. A progressive increase in IECs of total and phosphorylated IRE1α (encoded by *Ern1*), the sensor of ER stress upstream of XBP1 and known to control NFκB[27] was observed in $Atg16l1^{\Delta IEC}$, $Xbp1^{\Delta IEC}$ and $Atg16l1/Xbp1^{\Delta IEC}$ in comparison to *Wt* mice (Fig. 3f) and mirrored the escalating elevations in NFκB (Fig. 3b and Extended Data Fig. 6e, f). Indeed, increased NFκB activity and ileitis were governed by IRE1α as the increased epithelial NFκB phosphorylation observed in $Xbp1^{\Delta IEC}$ mice was abrogated in $Ern1/Xbp1^{\Delta IEC}$ mice (Fig 3g), *Ern1* co-silencing of *shXbp1* MODE-K cells abolished increased expression of the NFκB target gene *Nfkbia* in response to TNF stimulation relative to *shCtrl* MODE-K cells (Extended Data Fig. 6k), and enteritis was diminished in $Ern1/Xbp1^{\Delta IEC}$ compared to $Xbp1^{\Delta IEC}$ mice (Fig. 3h). Enteritis was also reversed by germline deletion of *Tnfrsf1a* in $Xbp1^{\Delta IEC}$ mice (Fig. 3i), and re-derivation of $Xbp1^{\Delta IEC}$ mice into a germ-free environment (Fig. 3j), which was associated with reduced p-IκBα immunoreactivity in *Xbp1*-deficient IECs compared to mice housed under SPF conditions (Fig. 3k). These studies together demonstrate that enteritis in this model is driven by TNF, the cytokine targeted by the most potent therapeutics of human CD[25], and microbes in a pathway that derives from IEC death and IRE1α-dependent activation of NFκB with ATG16L1-dependent autophagy serving to restrain the inflammatory nature of the latter likely through its removal.

Accordingly, treatment of $Xbp1^{T\text{-}\Delta IEC}$ mice with the mTOR inhibitor rapamycin[10] induced autophagy primarily in crypts (Extended Data Fig. 7a, b), diminished IEC-associated NFκB activation and number of $TUNEL^{+}$ IECs in $Xbp1^{\Delta IEC}$ mice (Fig. 4a and Extended Data Fig. 7c-e), and markedly reduced the severity of enteritis (Fig. 4b). These beneficial consequences of rapamycin in the setting of unabated ER stress in IECs were not observed in $Atg7/Xbp1^{\Delta IEC}$ and $Atg16l1/Xbp1^{\Delta IEC}$ mice (Extended Data Fig. 7e-i), demonstrating that these effects required intact autophagy within IECs.

The spatial convergence of the consequences of hypomorphic UPR and autophagy function in Paneth cells prompted us to test the hypothesis that these pathways were interdependent in this cell type. We developed a *defensin 6 alpha* promoter[28]-driven *Cre* transgenic line (*D6-Cre*), and confirmed the exclusive activity of Cre recombinase in $lysozyme^{+}$ Paneth cells (Fig. 4c). Paneth cell-specific deletion of *Xbp1* in $D6\text{-}Cre;Xbp1^{fl/fl}$ (‘$Xbp1^{\Delta PC}$’) mice resulted in autophagy activation (Fig. 4d and Extended Data Fig. 8a, b) and structural defects in granule morphology in Paneth cells (Fig. 4e, f). Crypts of $Xbp1^{\Delta PC}$ compared to *Wt* mice exhibited increased GRP78 expression (Fig. 4d and Extended Data Fig. 8b) and p-eIF2α immunoreactivity (Fig. 4g), accompanied by increased conversion of LC3-I/II and reduced p62 levels (Fig. 4d and Extended Data Fig. 8b), demonstrating ER stress and autophagy induction. Strikingly, 75% of these mice developed spontaneous enteritis (Fig. 4h, i) that shared the characteristics with $Xbp1^{\Delta IEC}$ mice (Fig. 2b). $Xbp1^{\Delta PC}$ mice exhibited increased cell death in crypts (Extended Data Fig. 9a, b) and IEC turnover (Extended Data Fig. 9c-f), while goblet cells remained unaffected (Extended Data Fig. 9g, h). Notably, $Atg7/Xbp1^{\Delta PC}$ mice exhibited transmural disease as early as 8 weeks of age (Extended Data Fig. 9i). We conclude that deletion of *Xbp1* specifically in Paneth cells results in unresolved ER stress, UPR activation and induction of autophagy which can serve as a nidus for the emergence of spontaneous intestinal inflammation that evolves into transmural disease in the absence of the compensation provided by autophagy.

Our studies thus support a mechanistic model (Extended Data Fig. 10a-c) for how *ATG16L1*-associated genetic risk may convert into a disease phenotype. The competence of the UPR likely sets the threshold for susceptibility of the host with hypofunctional autophagy to interacting genetic and environmental factors capable of inducing inflammation. Consistent with our model, patients with CD carrying the *ATG16L1*^{T300A} risk variant, which impairs autophagosome formation[29], frequently exhibit ER stress in their Paneth cells, in contrast to those harbouring the normal variant[30]. Finally, our studies also unequivocally establish that these inflammatory susceptibilities can emerge directly from highly secretory Paneth cells and suggest that small intestinal CD may be a specific disorder of this cell type.

Methods

Mice

Xbp1$^{fl/fl}$ mice were crossed with *V-Cre-ER*$^{T2+}$ (B6) mice kindly provided by Drs. Nicholas Davidson (Washington University, St. Louis) and Sylvie Robine (Institut Curie-CNRS, Paris) to generate mice with tamoxifen inducible *Xbp1* deletion in the intestinal epithelium (‘*Xbp1*$^{T\text{-}\Delta IEC}$’). *V-Cre-ER*$^{T2+}$ recombinase was activated by 3 or 5 daily intraperitoneal administrations of 1 mg tamoxifen (MP Biomedicals) as indicated in figure legends. *V-Cre*$^{+}$*;Xbp1*$^{fl/fl}$ (‘*Xbp1*$^{\Delta IEC}$’) mice were crossed with *Atg7*$^{fl/fl}$ mice[14] kindly provided by Dr. Komatsu, Tokyo Metropolitan Institute of Medical Science, Tokyo, to obtain *V-Cre*$^{+}$*;Atg7*$^{fl/fl}$*;Xbp1*$^{fl/fl}$ (‘*Atg7/Xbp1*$^{\Delta IEC}$’) mice. Mice with a floxed *Atg16l1* allele were generated in collaboration with GenOway, France. Briefly, a proximal *loxP* site was introduced within the promoter region of *Atg16l1* gene upstream of exon 1, a distal loxP site was introduced with an FRT flanked neomycin selection cassette within intron 1. The resultant mouse line was bred with deleter-mice constitutively expressing Flp-recombinase to remove the neomycin selection cassette, creating an *Atg16l1*$^{fl/+}$ mouse in which *Atg16l1* exon 1 was flanked by two *loxP* sites (Extended Data Fig. S4g). After backcrossing onto B6, these mice were crossed with *V-Cre*$^{+}$ mice[31] resulting in *V-Cre;Atg16l1*$^{fl/fl}$ mice with IEC-specific *Atg16l1* deletion (‘*Atg16l1*$^{\Delta IEC}$’). *Atg16l1*$^{fl/fl}$ mice were crossed with *Xbp1*$^{\Delta IEC}$ mice to develop *V-Cre*$^{+}$*;Atg16l1*$^{fl/fl}$*;Xbp1*$^{fl/fl}$ (‘*Atg16l1/Xbp1*$^{\Delta IEC}$’) mice. *GFP-LC3* transgenic mice[12], generous gift of Dr. Mizushima, Tokyo Medical and Dental University, Tokyo, were crossed with *V-Cre-ER*$^{T2+}$*;Xbp1*$^{fl/fl}$ to generate *GFP-LC3;V-Cre-ER*$^{T2+}$*;Xbp1*$^{fl/fl}$ mice (‘*GFP-LC3;Xbp1*$^{T\text{-}\Delta IEC}$’). For the generation of Paneth cell-specific *Defa6-Cre;Xbp1*$^{fl/fl}$ mice, a 1.1 kb cDNA fragment encoding improved Cre (iCre)[32] recombinase was subcloned downstream of nucleotides −6500 to +34 of mouse cryptdin-2 gene (*Defa6*) in the *BamHI* site of the pCR2-TAg-hGH plasmid[33,34] to replace the DNA fragment containing the simian virus 40 large antigen (SV40). A linearized 10.2 kb fragment containing the *Defa6* promoter, iCre and hGH (*Defa6-iCre-hGH*) was removed by *EcoRI* digestion, agarose gel-electrophoresed and purified with QIAEX Gel Extraction Kit (Qiagen), and used for pronuclear injection of BL/6 mice. Six founders from 22 live born mice were identified by screening tail DNA using iCre-specific primers, and two lines were further characterized and crossed to *Xbp1*$^{fl/fl}$ and *EYFP-Rosa26* reporter mice[35], kindly provided by K. Rajewsky. *Gadd34*$^{-/-}$ mice[16] were crossed with *V-Cre;Xbp1*$^{fl/fl}$ mice to generate *V-Cre;Xbp1*$^{fl/fl}$*;Gadd34*$^{+/-}$ (‘*Xbp1*$^{\Delta IEC}$*;Gadd34*$^{+/-}$’) mice. *Ern1*$^{fl/f}$ [36] and *Tnfrsf1a*$^{-/-}$ (Jackson) mice were crossed with *V-Cre;Xbp1*$^{fl/fl}$ mice to generate *V-Cre;Ern1*$^{fl/fl}$*;Xbp1*$^{fl/fl}$ (‘*Ern1/Xbp1*$^{\Delta IEC}$’) and *V-Cre;Xbp1*$^{fl/fl}$*;Tnfrsf1a*$^{-/-}$ (‘*Xbp1*$^{\Delta IEC}$*;Tnfrsf1a*$^{-/-}$’) mice, respectively. *Cre* transgenes were maintained in the hemizygous state in all experimental strains with a floxed allele to generate littermate controls. *Xbp1*$^{\Delta IEC}$ mice were re-derived in a germ-free environment and housed in sterile isolators at the Taconic Farms breeding facility (Germantown, NY, USA). Tail or ear biopsy genomic DNA was used for genotyping of respective mouse strains as described

previously[4]. Primer sequences are available upon request. Mice were housed in specific pathogen free (SPF) barrier facilities at Harvard Medical School (*Atg7/Xbp1*$^{\Delta IEC}$ mice, *Atg7/Xbp1*$^{\Delta PC}$, *Xbp1*$^{\Delta PC}$, *GFP-LC3;Xbp1*$^{T\text{-}\Delta IEC}$, *Ern1/Xbp1*$^{\Delta IEC}$ and their respective controls), University of Cambridge (*Atg16l1/Xbp1*$^{\Delta IEC}$, *Xbp1*$^{\Delta IEC}$*/Gadd34*$^{+/-}$, *Ern1/Xbp1*$^{\Delta IEC}$ mice and their respective controls), Innsbruck Medical University (*Atg16l1/Xbp1*$^{\Delta IEC}$, *Xbp1*$^{\Delta IEC}$*;Tnfrsf1a*$^{-/-}$, *Xbp1*$^{T\text{-}\Delta IEC}$ mice and their respective controls), and Christian-Albrechts-Universität zu Kiel (*Atg16l1*$^{\Delta IEC}$ mice and their respective controls). Colonies maintained at Boston and Innsbruck were murine norovirus (MNV) positive by Taqman qRT-PCR (Extended Data Fig. 9j). *Xbp1*$^{\Delta IEC}$, *Atg16l1*$^{\Delta IEC}$, *Ern1*$^{\Delta IEC}$ and their associated double-mutant strains were re-derived from the Innsbruck colony into the MNV-free enhanced barrier Cambridge facility, and colonies confirmed MNV-negative by PCR (Extended Data Fig. 9j) and serology (data not shown), as were *Atg16l1*$^{\Delta IEC}$ mice held at the Kiel facility. MNV Taqman qRT-PCR was performed as described[37]. The phenotype of single- and double-mutant colonies that had been re-derived from the MNV^{+} Innsbruck facility into the MNV^{-} Cambridge facility were indistinguishable, in particular relating to qualitative and quantitative measures of enteritis and the reciprocal induction of autophagy and ER stress. Mice were handled and all experiments performed in accordance with institutional guidelines and with the approval of the relevant authorities. 8-10 week old mice were used for all experiments unless stated otherwise in the figure legend, and were randomly allocated into treatment groups.

Antibodies and reagents

The following antibodies and reagents were used for immunoblotting: Sigma Aldrich: anti-LC3B (L7543). Cell Signaling Technology: anti-β-actin (4970; 13E5) anti-GAPDH (2118; 14C10), anti-eIF2α (9722), anti-phospho-eIF2α (3597; 119A11), anti-PERK (3192; C33E10), anti-phospho-PERK (3179; 16F8), anti-JNK (9252), anti-phospho-JNK (4668; 81E11), anti-ATG5 (8540; D1G9), anti-Beclin-1 (3495; D40C5), anti-ATG7 (8558; D12B11), anti-CHOP (5554; D46F1), anti-ATG12 (4180; D88H11), anti-p62 (5114), anti-IKK1 (2682), anti-IKK2 (2370; 2C8), anti-phospho-IKK1/2 (2697; 16A6), anti-IRE1α (3294; 14C10), anti-phospho-NFκB p65 (33033; 93H1), anti-NFκB p65 (4764; C22B4) and anti-rabbit/mouse HRP antibodies (7074, 7076). Abcam: anti-phospho-IRE1α (48187). MBL: anti-ATG16L1 (M150-3; 1F12). Stressgen: anti-heme-oxygenase-1 (ADI-SPA-895). Novus Biologicals: anti-GRP78 (NBP1-06274). Santa Cruz Biotechnology: anti-ATF4 (sc-200; C20). Immunoprecipitation antibody: anti-IRE1α (Santa Cruz Biotechnology, 20790; H190). Immunohistochemistry antibodies: Santa Cruz Biotechnology: anti-Lysozyme (27958; C19), MBL: anti-ATG16L1 (M150-3; 1F12). Cell Signaling Technology: anti-ATG16L1 (8089; D6D5), anti-phospho-IκBα (2859; 14D4), anti-phospho-eIF2α (3597; 119A11). Abcam: anti-Ki67 (15580), anti-GRP78 (21685). Progen: anti-p62 (GP62-C). BD Bioscience: anti-BrdU (551321).

The following reagents were used: TNF (Peprotech, 315-01A), Bafilomycin A1 (Sigma Aldrich, B1793), rapamycin (LC Laboratories, R-5000), JNK inhibitor (Sigma Aldrich, SP600125), NFκB inhibitor (Calbiochem, BAY11-7082) and salubrinal (Alexis Biochemicals, ALX-270-428) were dissolved in DMSO as recommended. *N*-acetyl cysteine (Sigma Aldrich, A9165) and glutathione (Calbiochem, NOVG3541) were used at final concentration of 1mM. Ambion siRNA for *Atg16l1* (94892, sense: GAACUGUUAGGGAAGAUCATT, antisense: UGAUCUUCCCUAACAGUUCCA), *Perk* (65405, sense: CCCGAUAUCUAACAGAUUUTT, antisense: AAAUCUGUUAGAUAUCGGGAT; 65406, sense: CGAAGAAUACAGUAAUGGUTT, antisense: ACCAUUACUGUAUUCUUCGTG), *Gadd34* (70230, sense: CCAUAGCUCCGGGAUACAATT, antisense: UUGUAUCCCGGAGCUAUGGAA; 70231, sense: AGACAACAGCGAUUCGGAUTT, antisense:

AUCCGAAUCGCUGUUGUCUTC), *Ern1* (95857, sense: GUUUGACCCUGGACUCAAATT, antisense: UUUGAGUCCAGGGUCAAACTT; 95858, sense: GGAUGUAAGUGACCGAAUATT, antisense: UAUUCGGGUCACUUACAUCCTG; 95859, sense: GCUCGUGAAUUGAUAGAGATT, antisense: UCUCUAUCAAUUCACGAGCAA) and scrambled control were used at a final concentration of 10μM.

Chromatin Immunoprecipitation (ChIP)

ChIP with anti-ATF4 and control IgG rabbit antibody was performed in *Xbp1* and control silenced MODE-K cells according to ChIP protocol by Agilent. To determine the presence of ATF4 binding sites in the *Atg7* promoter, a 4-kb region proximal to transcription start site identified with the Eukaryotic Promoter Database Primers was analyzed using MatInspector (Genomatix). Immunoprecipitated DNA was subject to quantitative PCR (qPCR) to determine enrichment of ATF4 binding to respective promoters and results were normalized to input chromatin DNA. Primers used for qPCR were as follows for *Map1LC3b*[13], for *Atg7* F 5'-GCGCTTCCGCGTTTGTGTGG and R 5'CTGCTCCGCAACCACGGCTT.

Salubrinal, rapamycin and BAY11-7082 treatment in vivo

Salubrinal [1mg/kg/d], rapamycin [1.5mg/kg/d] or vehicle (DMSO) was administered intraperitoneally (i.p.) 24h prior to the first tamoxifen administration to *GFP-LC3;V-CreER*^{T2};*Xbp1*$^{fl/fl}$ (*GFP-LC3;Wt*) and *GFP-LC3;Xbp1*$^{T\text{-}\Delta IEC}$ mice. 3-day treatment was used for evaluation of accumulation of GFP-LC3 punctae in the intestinal epithelium, while a 5-day combined tamoxifen and salubrinal treatment followed by two daily salubrinal injections was used in experiments with enteritis assessment as an end point (Extended Data Fig. 2a and 3g). To assess the effects of rapamycin on ER stress-induced intestinal inflammation in XBP1 deficiency, *V-Cre;Xbp1*$^{fl/fl}$ (*Xbp1*$^{\Delta IEC}$), V-*Cre;Atg16l1*$^{fl/fl}$;*Xbp1*$^{fl/fl}$ or V-*Cre;Atg7*$^{fl/fl}$;*Xbp1*$^{fl/fl}$ and the respective control mice were treated with rapamycin or vehicle for 14 consecutive days i.p. and inflammation was evaluated. BAY11-7082[38] or vehicle (DMSO) was administered intraperitoneally (i.p.) every other day at 5mg/kg for 14 consecutive days in *Xbp1*$^{\Delta IEC}$ mice, or for 5 consecutive days at 20mg/kg in *Xbp1*$^{T\text{-}\Delta IEC}$ mice concomitant with i.p. tamoxifen.

Transmission electron microscopy

Small intestinal tissue from mice was handled by standard methods to be fixed with 1.25% glutaraldehyde, 4% formaldehyde in 0.1 M cacodylate buffer at pH 7.4 at room temperature for electron microscopy. The detailed procedures for electron microscopy was previously described[39] and the tissue was observed with a JEOL 1400 transmission electron microscope at 120 kV operating voltage. For quantification of autophagy, number of autophagic vacuoles was manually counted by TEM expert (J.H.) blinded to sample identity in 10 consecutive Paneth cells per sample. ImageJ software was used to measure average size of autophagic vacuoles.

Histology

Formalin-fixed and paraffin-embedded intestinal tissue was sectioned and stained with hematoxylin and eosin (H&E) as previously described[4]. A semi-quantitative composite scoring system was used for the assessment of spontaneous intestinal inflammation, computed as a sum of five histological subscores, multiplied by a factor based on the extent of the inflammation. Histological subscores (for each parameter: 0, absent; 1, mild; 2, moderate; 3, severe): mononuclear cell infiltrate (0-3), crypt hyperplasia (0-3), epithelial injury/erosion (0-3), polymorphonuclear cell infiltrates (0-3) and transmural inflammation (0, absent; 1, submucosal; 2, one focus extending into muscularis and serosa; 3 up to five

foci extending into muscularis and serosa; 4, diffuse). Extent factor was derived according to the fraction of bowel length involved by inflammation: 1, < 10%, 2, 10-25%, 3, 25-50% and 4, >50%. Ileal inflammation was assessed by an expert gastrointestinal pathologist (J.N.G.) who was blinded to the genotype and experimental conditions of the samples. No spontaneous colonic inflammation was detected in any of the reported genotypes.

Reactive oxygen species (ROS), cell death detection by flow cytometry and NFκB activity assays

To evaluate oxidative stress, *Xbp1*- and control-silenced MODE-K cells[40] were incubated with 5 μM 5-(and-6)-chloromethyl-2',7'-dichlorodihydrofluorescein diacetate, acetyl ester (CM-H2DCFDA) (Molecular Probes) for 30 min[41]. After washing with PBS, cells were further incubated with complete medium for 2 hours. ROS generation was determined using flow cytometry. To evaluate cell death, *shXbp1* and *shCtrl* cells were co-silenced for *Atg16l1* using siRNA or scrambled control (Ambion). After 4 days, cells were harvested and stained for Annexin V (Biolegend, UK) in staining buffer (Biolegend, UK) and mode of cell death was determined by flow cytometry after addition of propidium iodide (PI). To assess NFκB signaling pathway activation, *Xbp1*- or control-silenced MODE-K cells were stimulated with 50ng/ml TNF for indicated periods of time, followed by immunoblotting (using NE-PER [Thermo Scientific] isolated cytoplasmic extracts), qRT-PCR, and chemiluminescent detection of NFκB consensus sequence binding activity with the NFκB p65 transcription factor assay kit (Thermo Scientific). *Ern1* or scrambled siRNA (Ambion) was used for co-silencing as indicated.

Immunohistochemistry, bromodeoxyuridine (BrdU) and terminal deoxinucleotidyl transferase (TUNEL) labeling

Formalin fixed paraffin embedded sections were stained according to standard immunohistochemistry protocols and manufacturer's recommendations as described previously[4]. Cell death was assessed by TUNEL labeling of formalin fixed paraffin embedded slides of the respective genotypes using the TUNEL cell death detection kit (Roche). Entire slides were analyzed for $TUNEL^+$ cells and numbers normalized to intestinal length on the slide. Proliferation of the intestinal epithelium was assessed after a 24h pulse with BrdU (BD Pharmingen) and incorporated BrdU was detected by the BrdU in situ detection kit (BD Pharmingen). $BrdU^+$ nuclei per total IECs along the crypt villus axis are shown. Toluidine blue staining and Periodic acid-Schiff (PAS) reaction was performed according to standard protocols.

Confocal microscopy for detection of GFP-LC3 and EYFP

For detection of GFP-LC3 or EYFP, mice were euthanized, followed by transcardiac perfusion with PBS (2-3 minutes) and 3.7 % formaldehyde (3-4 minutes). Small intestine was dissected and promptly washed with PBS. The tissue was fixed in formalin for an additional 12-18 hours. Fixed tissue was embedded in OCT and sectioned on a cryotome into 5μm sections. Slides were washed with PBS and Prolong Gold Antifade reagent with DAPI (Invitrogen) with application of an attached coverglass. Images of the sections were collected using Olympus semi-confocal system. MetaMorph software was used for image analysis. For the detection of autophagosome formation in vitro, *Xbp1* and control silenced MODE-K cells were transfected with a GFP-LC3 plasmid[12] (a kind gift of Dr. Noboru Mizushima, Tokyo Medical and Dental University) with use of Lipofectamine LTX (Invitrogen) following the manufacturer's instructions. Accumulation of GFP-LC3 punctae or EYFP signal was assessed using LSM510 META Confocal Microscopy (Carl Zeiss).

Intestinal epithelial cell purification and crypt isolation

Mice were euthanized and the intestine was washed with ice-cold PBS after being cut open longitudinally. Peyer's patches were removed and the intestine was cut into small pieces. Mucus was removed by shaking the intestine in 1x HBSS containing 1mM DTT for 10 min at RT. After washing with PBS, pieces were digested with Dispase (1U/ml in RPMI with 2% FCS) for 30 min at 37 degree with shaking (250 rpm). Cells were collected and debris removed with a 100μm cell strainer, and centrifuged for 5 min at 1500rpm. IECs were collected in the top layer after 40% - 100% Percoll gradient centrifugation. Purity of the population was determined by staining with anti-EpCAM antibody and flow cytometry analysis. IECs were lysed with RIPA buffer and equal amounts of protein were used for western blot analysis as indicated in figure legends. To isolate small intestinal crypts, the intestine was flushed, cut open longitudinally and incubated on ice for 30 minutes in 2mM EDTA/PBS. Two sedimentation steps and application of a cell strainer separated crypts from villi[42], which were then used for RNA isolation (Qiagen), *Xbp1* splicing assay, and for protein lysis with RIPA buffer and subsequent immunoblotting.

Intestinal epithelial scrapings

Mice were euthanized, intestines collected and longitudinally opened, and immediately washed with ice-cold PBS. Intestinal epithelium was collected by scraping with glass slides and snap frozen into liquid nitrogen for further analysis. For protein analysis, intestinal epithelial scrapings were homogenized in RIPA buffer using a 25G needle with a syringe. Lysates were cleared by centrifugation and aliquots of protein were used for protein assessment using standard western blot or immunoprecipitation protocols as indicated. Isolation of mRNA from intestinal epithelial scrapings or MODE-K lysates and RT-qPCR was performed as described[4] using following pairs of primers. *grp78* 5-ACTTGGGGACCACCTATTCCT and 5-ATCGCCAATCAGACGCTCC; *Gadd34* 5-CCCGAGATTCCTCTAAAAGC and 5-CCAGACAGCAAGGAAATGG; *LC3b* 5-GCGCCATGCCGTCCGAGAAG and 5-GCTCCCGGATGAGCCGGACA; *Xbp1* 5-ACACGCTTGGGAATGGACAC and 5-CCATGGGAAGATGTTCTGGG; *Atg7* 5-CCTTCGCGGACCTAAAGAAGT and 5-CCCGGATTAGAGGGATGCTC; *Nfkbia* 5-TGAAGGACGAGGAGTACGAGC and 5-TTCGTGGATGATTGCCAAGTG.

Dextran Sodium Sulfate induced colitis

Acute colitis was induced by adding 4% DSS (TdB Consultancy) to drinking water ad libitum for 5 consecutive days. Daily disease activity index (DAI) was assessed evaluating weight loss, stool consistency and rectal bleeding according to Table S1. A high resolution mouse endoscopic system (Hopkins, Germany) was used. Colitis severity was assessed by a semiquantitative score consisting of two subscores;endoscopic tissue damage (0-3, where 0 - no damage, 1 – lymphoepithelial lesions, 2- surface mucosal erosion or focal ulceration and 3 - extensive mucosal damage with expansion into deeper structures of the bowel wall) and inflammatory infiltration (0-3, where 0 – occasional inflammatory cells in the lamina propria, 1 – increased numbers on inflammatory cells in lamina propria, 2 – confluence of inflammatory cells extending into the submucosa and 3 – transmural extension of the infiltrate).

Xbp1 splicing assay and densitometric quantification

Xbp1 splicing was assessed as described[4]. Briefly, RNA was isolated, reverse transcribed and amplified by RT-PCR with the following primers: *Xbp1* sp F: ACACGCTTGGGAATGGACAC; *Xbp1* sp R: CCATGGGAAGATGTTCTGGG. The PCR product of 171 (unspliced) and 145 (spliced) bp were resolved on a 2% agarose gel. Densitometric analysis for splicing assay and immunoblots was performed with ImageJ.

Statistical methods

Statistical significance was calculated as appropriate using an unpaired two-tailed Student's *t*-test or a Mann-Whitney U test and considered significant at $p < 0.05$. In experiments where more than two groups were compared, Kruskal-Wallis test followed by Mann-Whitney U and post-hoc Bonferroni Holm's correction or one-way ANOVA/Bonferroni was performed. Grubb's test was used as appropriate to identify outliers. Data was analyzed using GraphPad Prism software. Experimental group sizes were based upon the goal of achieving desired effect sizes typically of ≤2.0 standard deviations and a power of 0.9 on the assumption of a normal distribution, and therefore typically involved n=6-10.

Supplementary Material

Refer to Web version on PubMed Central for supplementary material.

Acknowledgments

The authors wish to thank L. Glimcher, A. Goldberg, J. Yuan, M. Parkes and C.L. Bevins for thoughtful discussion of the project and are grateful to J. Gordon, L. Hooper and K. Rajewsky for providing critical reagents. This work was supported by NIH grants DK044319, DK051362, DK053056, DK088199, the Harvard Digestive Diseases Center (HDDC) (DK0034854) (R.S.B.); the European Research Council under the European Community's Seventh Framework Programme (FP7/2007-2013) / ERC Grant agreement n° 260961 (A.K.); the National Institute for Health Research Cambridge Biomedical Research Centre (A.K.); the Austrian Science Fund and Ministry of Science P21530-B18 and START Y446-B18 (A.K.); the Addenbrooke's Charitable Trust (A.K.); BMBF NGFN Animal Model grant (P.R.), the DFG Cluster of Excellence Inflammation at Interfaces; DFG grants RO2994/5-1 (S.S. & P.R.) and SFB 877 project B9 (P.R.); fellowships from Inflammatory Bowel Disease Working Group (M.F.T.), European Crohn's and Colitis Organization (T.E.A.), Crohn's in Childhood Research Association (L.N.), National Research Foundation of Korea funded by the Korean government KRF-2008-357-E00022 /No. 2011-0009018 (H.J.-K.).

References

1. Jostins L, et al. Host-microbe interactions have shaped the genetic architecture of inflammatory bowel disease. Nature. 2012; 491:119–124. [PubMed: 23128233]
2. Cadwell K, et al. A key role for autophagy and the autophagy gene Atg16l1 in mouse and human intestinal Paneth cells. Nature. 2008; 456:259–263. [PubMed: 18849966]
3. Cadwell K, et al. Virus-plus-susceptibility gene interaction determines Crohn's disease gene Atg16L1 phenotypes in intestine. Cell. 2010; 141:1135–1145. [PubMed: 20602997]
4. Kaser A, et al. XBP1 links ER stress to intestinal inflammation and confers genetic risk for human inflammatory bowel disease. Cell. 2008; 134:743–756. [PubMed: 18775308]
5. Treton X, et al. Altered endoplasmic reticulum stress affects translation in inactive colon tissue from patients with ulcerative colitis. Gastroenterology. 2011; 141:1024–1035. [PubMed: 21699776]
6. Kobayashi KS, et al. Nod2-dependent regulation of innate and adaptive immunity in the intestinal tract. Science. 2005; 307:731–734. [PubMed: 15692051]
7. Zheng W, et al. Evaluation of AGR2 and AGR3 as candidate genes for inflammatory bowel disease. Genes Immun. 2006; 7:11–18. [PubMed: 16222343]
8. Wehkamp J, et al. Reduced Paneth cell alpha-defensins in ileal Crohn's disease. Proc Natl Acad Sci U S A. 2005; 102:18129–18134. [PubMed: 16330776]
9. Maloy KJ, Powrie F. Intestinal homeostasis and its breakdown in inflammatory bowel disease. Nature. 2011; 474:298–306. [PubMed: 21677746]
10. Levine B, Mizushima N, Virgin HW. Autophagy in immunity and inflammation. Nature. 2011; 469:323–335. [PubMed: 21248839]
11. Sarkar S, Ravikumar B, Rubinsztein DC. Autophagic clearance of aggregate-prone proteins associated with neurodegeneration. Methods Enzymol. 2009; 453:83–110. [PubMed: 19216903]

12. Mizushima N, Yamamoto A, Matsui M, Yoshimori T, Ohsumi Y. In vivo analysis of autophagy in response to nutrient starvation using transgenic mice expressing a fluorescent autophagosome marker. Mol Biol Cell. 2004; 15:1101–1111. [PubMed: 14699058]
13. Rouschop KM, et al. The unfolded protein response protects human tumor cells during hypoxia through regulation of the autophagy genes MAP1LC3B and ATG5. J Clin Invest. 2010; 120:127–141. [PubMed: 20038797]
14. Komatsu M, et al. Impairment of starvation-induced and constitutive autophagy in Atg7-deficient mice. J Cell Biol. 2005; 169:425–434. [PubMed: 15866887]
15. Boyce M, et al. A selective inhibitor of eIF2alpha dephosphorylation protects cells from ER stress. Science. 2005; 307:935–939. [PubMed: 15705855]
16. Novoa I, et al. Stress-induced gene expression requires programmed recovery from translational repression. EMBO J. 2003; 22:1180–1187. [PubMed: 12606582]
17. Hampe J, et al. A genome-wide association scan of nonsynonymous SNPs identifies a susceptibility variant for Crohn disease in ATG16L1. Nat Genet. 2007; 39:207–211. [PubMed: 17200669]
18. Cleynen I, et al. Genetic factors conferring an increased susceptibility to develop Crohn's disease also influence disease phenotype: results from the IBDchip European Project. Gut. 2012
19. Fujita N, et al. The Atg16L complex specifies the site of LC3 lipidation for membrane biogenesis in autophagy. Mol Biol Cell. 2008; 19:2092–2100. [PubMed: 18321988]
20. Mizushima N, et al. Mouse Apg16L, a novel WD-repeat protein, targets to the autophagic isolation membrane with the Apg12-Apg5 conjugate. J Cell Sci. 2003; 116:1679–1688. [PubMed: 12665549]
21. Fujita N, et al. Differential involvement of Atg16L1 in Crohn disease and canonical autophagy: analysis of the organization of the Atg16L1 complex in fibroblasts. J Biol Chem. 2009; 284:32602–32609. [PubMed: 19783656]
22. Yang L, Li P, Fu S, Calay ES, Hotamisligil GS. Defective hepatic autophagy in obesity promotes ER stress and causes insulin resistance. Cell metabolism. 2010; 11:467–478. [PubMed: 20519119]
23. Bertolotti A, et al. Increased sensitivity to dextran sodium sulfate colitis in IRE1beta-deficient mice. J Clin Invest. 2001; 107:585–593. [PubMed: 11238559]
24. Cao SS, et al. The unfolded protein response and chemical chaperones reduce protein misfolding and colitis in mice. Gastroenterology. 2013; 144:989–1000. e1006. [PubMed: 23336977]
25. Kaser A, Zeissig S, Blumberg RS. Inflammatory bowel disease. Annu Rev Immunol. 2010; 28:573–621. [PubMed: 20192811]
26. Rogler G, et al. Nuclear factor kappaB is activated in macrophages and epithelial cells of inflamed intestinal mucosa. Gastroenterology. 1998; 115:357–369. [PubMed: 9679041]
27. Kaneko M, Niinuma Y, Nomura Y. Activation signal of nuclear factor-kappa B in response to endoplasmic reticulum stress is transduced via IRE1 and tumor necrosis factor receptor-associated factor 2. Biol Pharm Bull. 2003; 26:931–935. [PubMed: 12843613]
28. Vaishnava S, Behrendt CL, Ismail AS, Eckmann L, Hooper LV. Paneth cells directly sense gut commensals and maintain homeostasis at the intestinal host-microbial interface. Proc Natl Acad Sci U S A. 2008; 105:20858–20863. [PubMed: 19075245]
29. Kuballa P, Huett A, Rioux JD, Daly MJ, Xavier RJ. Impaired autophagy of an intracellular pathogen induced by a Crohn's disease associated ATG16L1 variant. PLoS One. 2008; 3:e3391. [PubMed: 18852889]
30. Deuring JJ, et al. Genomic ATG16L1 risk allele-restricted Paneth cell ER stress in quiescent Crohn's disease. Gut. 2013 in press.
31. Madison BB, et al. Cis elements of the villin gene control expression in restricted domains of the vertical (crypt) and horizontal (duodenum, cecum) axes of the intestine. J Biol Chem. 2002; 277:33275–33283. [PubMed: 12065599]
32. Shimshek DR, et al. Codon-improved Cre recombinase (iCre) expression in the mouse. Genesis. 2002; 32:19–26. [PubMed: 11835670]
33. Garabedian EM, Roberts LJ, McNevin MS, Gordon JI. Examining the role of Paneth cells in the small intestine by lineage ablation in transgenic mice. J Biol Chem. 1997; 272:23729–23740. [PubMed: 9295317]

34. Bry L, et al. Paneth cell differentiation in the developing intestine of normal and transgenic mice. Proc Natl Acad Sci U S A. 1994; 91:10335–10339. [PubMed: 7937951]
35. Srinivas S, et al. Cre reporter strains produced by targeted insertion of EYFP and ECFP into the ROSA26 locus. BMC Dev Biol. 2001; 1:4. [PubMed: 11299042]
36. Iwawaki T, Akai R, Yamanaka S, Kohno K. Function of IRE1 alpha in the placenta is essential for placental development and embryonic viability. Proc Natl Acad Sci U S A. 2009; 106:16657–16662. [PubMed: 19805353]
37. Baert L, et al. Detection of murine norovirus 1 by using plaque assay, transfection assay, and real-time reverse transcription-PCR before and after heat exposure. Appl Environ Microbiol. 2008; 74:543–546. [PubMed: 18024676]
38. Pierce JW, et al. Novel inhibitors of cytokine-induced IkappaBalpha phosphorylation and endothelial cell adhesion molecule expression show anti-inflammatory effects in vivo. J Biol Chem. 1997; 272:21096–21103. [PubMed: 9261113]
39. Satoh Y, Yamano M, Matsuda M, Ono K. Ultrastructure of Paneth cells in the intestine of various mammals. J Electron Microsc Tech. 1990; 16:69–80. [PubMed: 2213233]
40. Vidal K, Grosjean I, evillard JP, Gespach C, Kaiserlian D. Immortalization of mouse intestinal epithelial cells by the SV40-large T gene. Phenotypic and immune characterization of the MODE-K cell line. J Immunol Methods. 1993; 166:63–73. [PubMed: 7693823]
41. Hempel SL, Buettner GR, O'Malley YQ, Wessels DA, Flaherty DM. Dihydrofluorescein diacetate is superior for detecting intracellular oxidants: comparison with 2',7'-dichlorodihydrofluorescein diacetate, 5(and 6)-carboxy-2',7'-dichlorodihydrofluorescein diacetate, and dihydrorhodamine 123. Free Radic Biol Med. 1999; 27:146–159. [PubMed: 10443931]
42. Sato T, et al. Single Lgr5 stem cells build crypt-villus structures in vitro without a mesenchymal niche. Nature. 2009; 459:262–265. [PubMed: 19329995]
43. Wei Y, Sinha S, Levine B. Dual role of JNK1-mediated phosphorylation of Bcl-2 in autophagy and apoptosis regulation. Autophagy. 2008; 4:949–951. [PubMed: 18769111]
44. Carchman EH, Rao J, Loughran PA, Rosengart MR, Zuckerbraun BS. Heme oxygenase-1-mediated autophagy protects against hepatocyte cell death and hepatic injury from infection/sepsis in mice. Hepatology. 2011; 53:2053–2062. [PubMed: 21437926]
45. Hu P, Han Z, Couvillon AD, Kaufman RJ, Exton JH. Autocrine tumor necrosis factor alpha links endoplasmic reticulum stress to the membrane death receptor pathway through IRE1alpha-mediated NF-kappaB activation and down-regulation of TRAF2 expression. Mol Cell Biol. 2006; 26:3071–3084. [PubMed: 16581782]
46. Urano F, et al. Coupling of stress in the ER to activation of JNK protein kinases by transmembrane protein kinase IRE1. Science. 2000; 287:664–666. [PubMed: 10650002]
47. Barrett JC, et al. Genome-wide association defines more than 30 distinct susceptibility loci for Crohn's disease. Nat Genet. 2008; 40:955–962. [PubMed: 18587394]
48. Tashiro E, et al. Trierixin, a novel Inhibitor of ER stress-induced XBP1 activation from Streptomyces sp. 1. Taxonomy, fermentation, isolation and biological activities. J Antibiot (Tokyo). 2007; 60:547–553. [PubMed: 17917237]
49. McKinney EF, et al. A CD8+ T cell transcription signature predicts prognosis in autoimmune disease. Nat Med. 2010; 16:586–591. 581p following 591. [PubMed: 20400961]
50. Rioux JD, et al. Genome-wide association study identifies new susceptibility loci for Crohn disease and implicates autophagy in disease pathogenesis. Nat Genet. 2007; 39:596–604. [PubMed: 17435756]
51. Parkes M, et al. Sequence variants in the autophagy gene IRGM and multiple other replicating loci contribute to Crohn's disease susceptibility. Nat Genet. 2007; 39:830–832. [PubMed: 17554261]

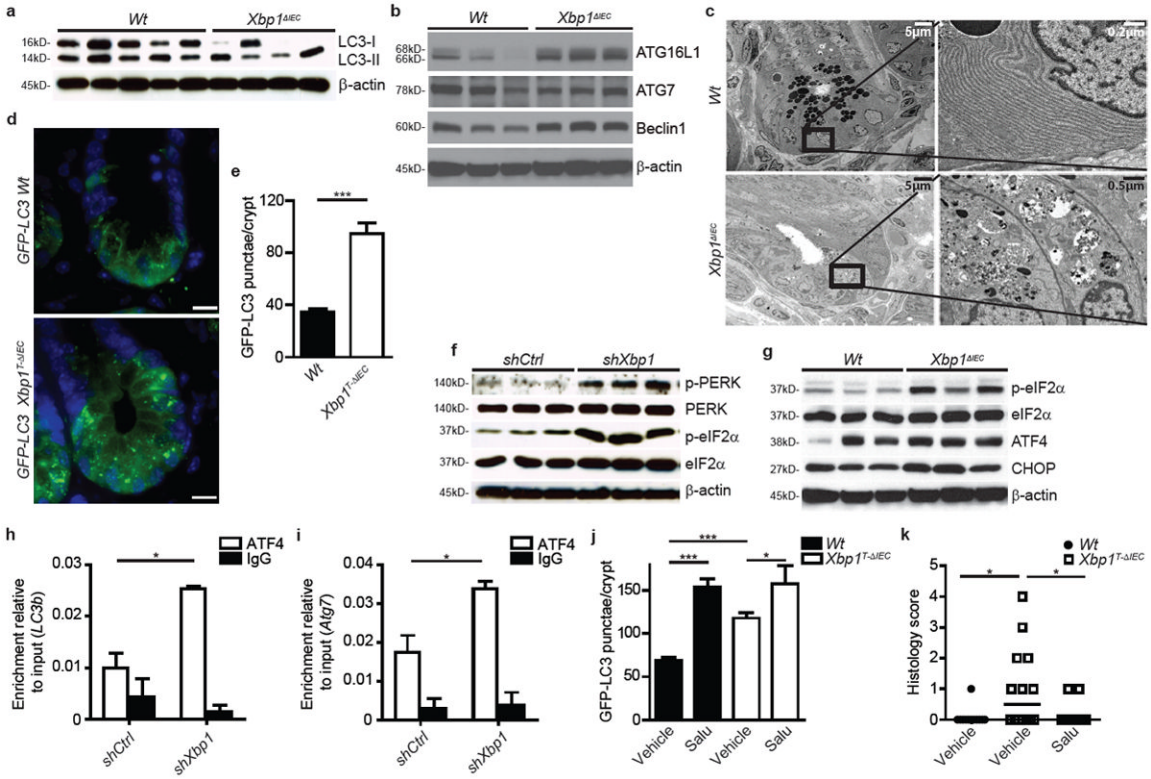

Figure 1. PERK/eIF2α signaling induces autophagy in *Xbp1*-deficient intestinal epithelial cells

a, b, Immunoblot for LC3 conversion in isolated primary IECs (**a**) (*n*=5/4) and for autophagy proteins in primary IEC scrapings (**b**) (*n*=3). **c,** Transmission electron microscopy (TEM) of crypts. Note autophagic vacuoles in various stages of evolution in *Xbp1*$^{\Delta IEC}$ hypomorphic Paneth cells. **d, e,** Crypt showing GFP-LC3 punctae (**d**), quantified in (**e**) (*n*=10; unpaired Student's t-test). Bar, 5 μm. **f, g,** Immunoblot of silenced MODE-K cells (**f**) and primary IEC scrapings (**g**) for the PERK/eIF2α branch (*n*=3). **h, i,** Promoter sequence qPCR for *Map1lc3b* (*LC3b*) (**h**) and *Atg7* (**i**) after anti-ATF4 ChIP (unpaired Student's t-test). **j,** GFP-LC3 punctae per crypt after treatment with tamoxifen for 3 days and vehicle or salubrinal (*n*=10; one-way ANOVA with post-hoc Bonferroni). (**k**) Enteritis histology score after salubrinal and tamoxifen co-treatment (*n*=12/14/13; median shown; Kruskal-Wallis with post-hoc Holm's-corrected Mann-Whitney U). Results represent three (**a, f, g**) or two (**c, e, h, i**) independent experiments. **P* < 0.05, ****P* < 0.001.

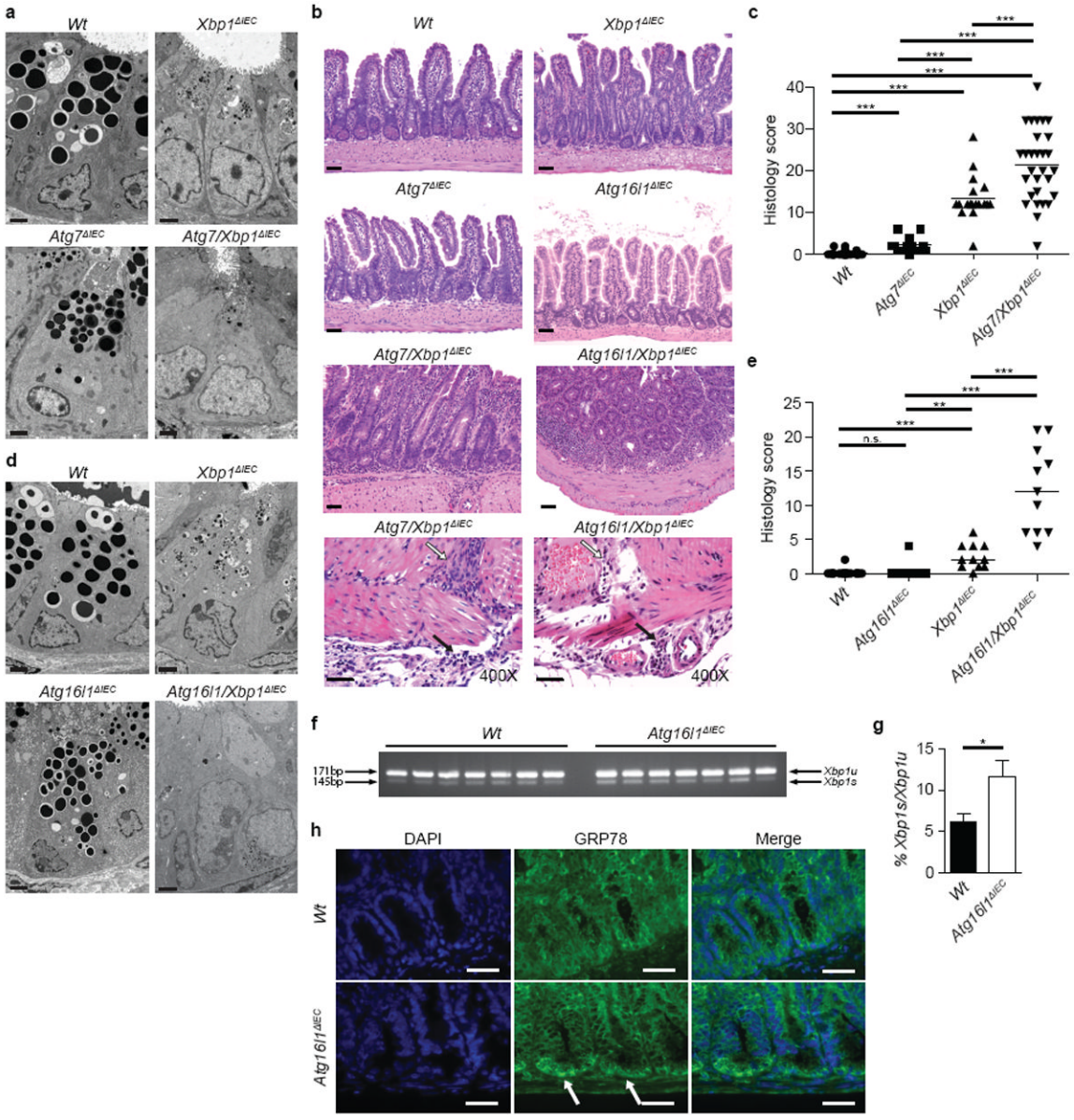

Figure 2. Impairment of ER stress-induced compensatory autophagy results in severe transmural inflammation

a, TEM of crypts of Lieberkühn (*n*=2). Bar, 2 μm. **b,** Representative H&E stainings. Note transmural inflammation extending through muscularis propria (white arrow) into serosa (black arrow) in *Atg7/Xbp1*$^{\Delta IEC}$ and *Atg16l1/Xbp1*$^{\Delta IEC}$ mice scored in (**c**) and (**e**). Bar, 50 and 10 μm, respectively. **c,** Enteritis histology score (*n*=26/12/18/27; 10-18 weeks; median shown; Kruskal-Wallis with post-hoc Holm's-corrected Mann-Whitney U). **d,** Crypt TEM in indicated genotypes (*n*=2). Bar, 2 μm. **e,** Enteritis histology score (*n*=11; 18 weeks; median shown; Kruskal-Wallis with post-hoc Holm's-corrected Mann-Whitney U). **f,** *Xbp1* mRNA splicing (*Xbp1u*, unspliced; *Xbp1s*, spliced) of crypts, densitometry in (**g**) (*n*=7; unpaired Student's t-test). **h,** GRP78 (green) immunofluorescence, white arrows indicate GRP78^{+} crypts (DAPI, blue; *n*=5). Bar, 10 μm. **P* < 0.05, ***P* < 0.01, ****P* < 0.001.

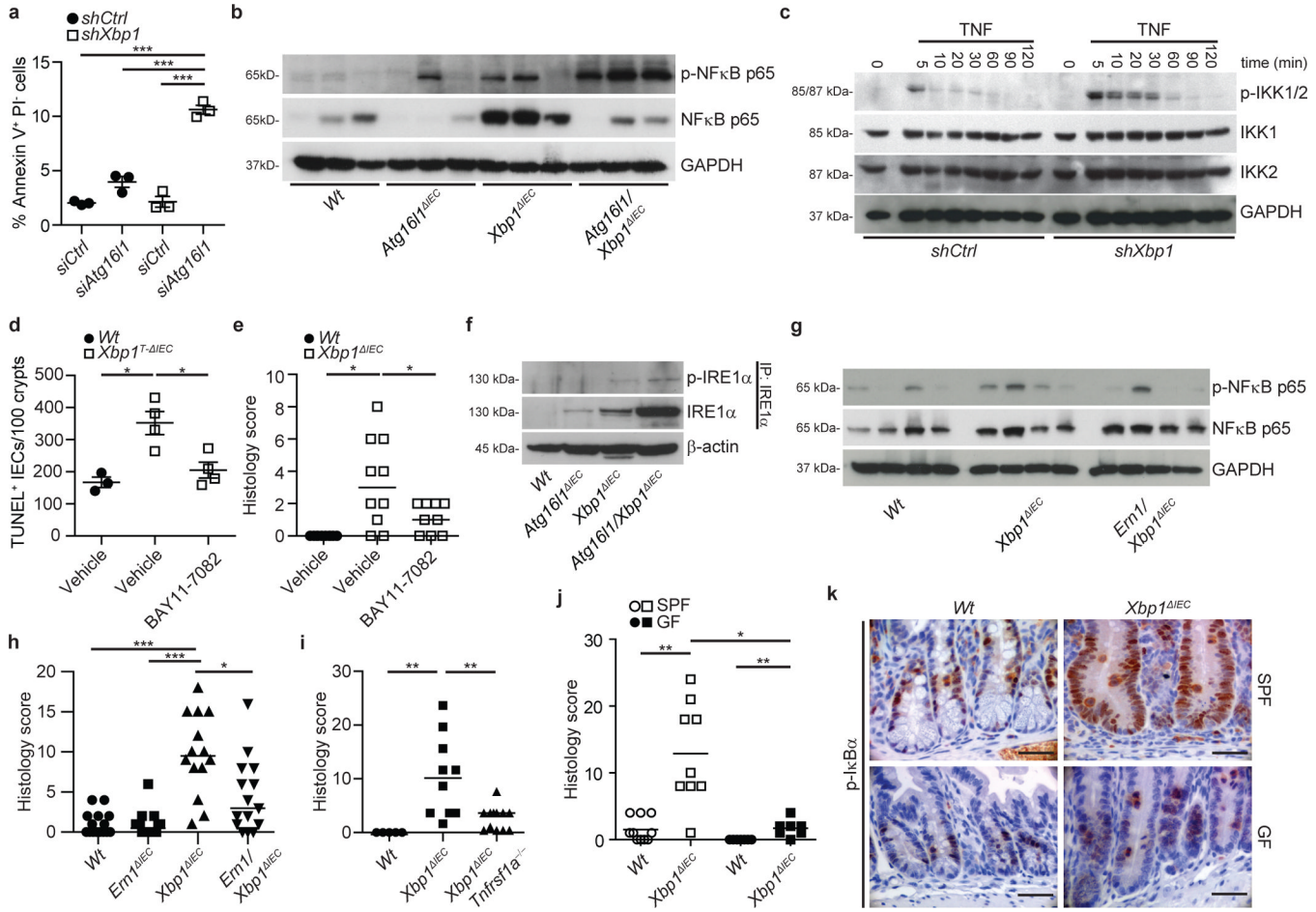

Figure 3. Autophagy restrains IRE1α-mediated NFκB activation in *Xbp1*-deficient epithelium

a, *shCtrl* or *shXbp1* MODE-K cells were co-silenced for *Atg16l1* (*siAtg16l1*) or with scrambled siRNA (*siCtrl*), and analyzed by flow cytometry for annexin V and propidium iodide (PI; one-way ANOVA with post-hoc Bonferroni). **b,** Immunoblot of primary IEC scrapings (n=3). **c,** Immunoblot of cytoplasmic extracts from *shCtrl* or *shXbp1* MODE-K cells after TNF stimulation. **d,** TUNEL$^+$ IECs per 100 crypts after BAY11-7082 or vehicle treatment (n=3/4/4; one-way ANOVA with post-hoc Holm's-corrected unpaired Student's t-test). **e,** Enteritis histology score of mice treated with BAY11-7082 or vehicle (n=10/10/9; median shown; Kruskal-Wallis with post-hoc Holm's-corrected Mann-Whitney U). **f,** Immunoblot of IEC scrapings for (p-)IRE1α after IRE1α immunoprecipitation (IP). β-actin, loading control of whole lysates. **g,** Immunoblot of primary IEC scrapings (n=4). **h, i,** Enteritis histology score of indicated genotypes (**h,** n=15/16/14/15; **i,** n=5/10/12; median shown; Kruskal-Wallis with post-hoc Holm's-corrected Mann-Whitney U). **j,** Enteritis histology score of specific pathogen free (SPF) and germ free (GF) housed mice (n=10/9/7/7; median shown; Kruskal-Wallis with post-hoc Holm's-corrected Mann-Whitney U). (**k**) Representative images of p-IκBα immunoreactivity under conditions as in (**j**) (n=4). Bar, 20 μm. Results represent four (**f**), three (**c**) or two (**a, b**) independent experiments. *P < 0.05, **P < 0.01, ***P < 0.001.

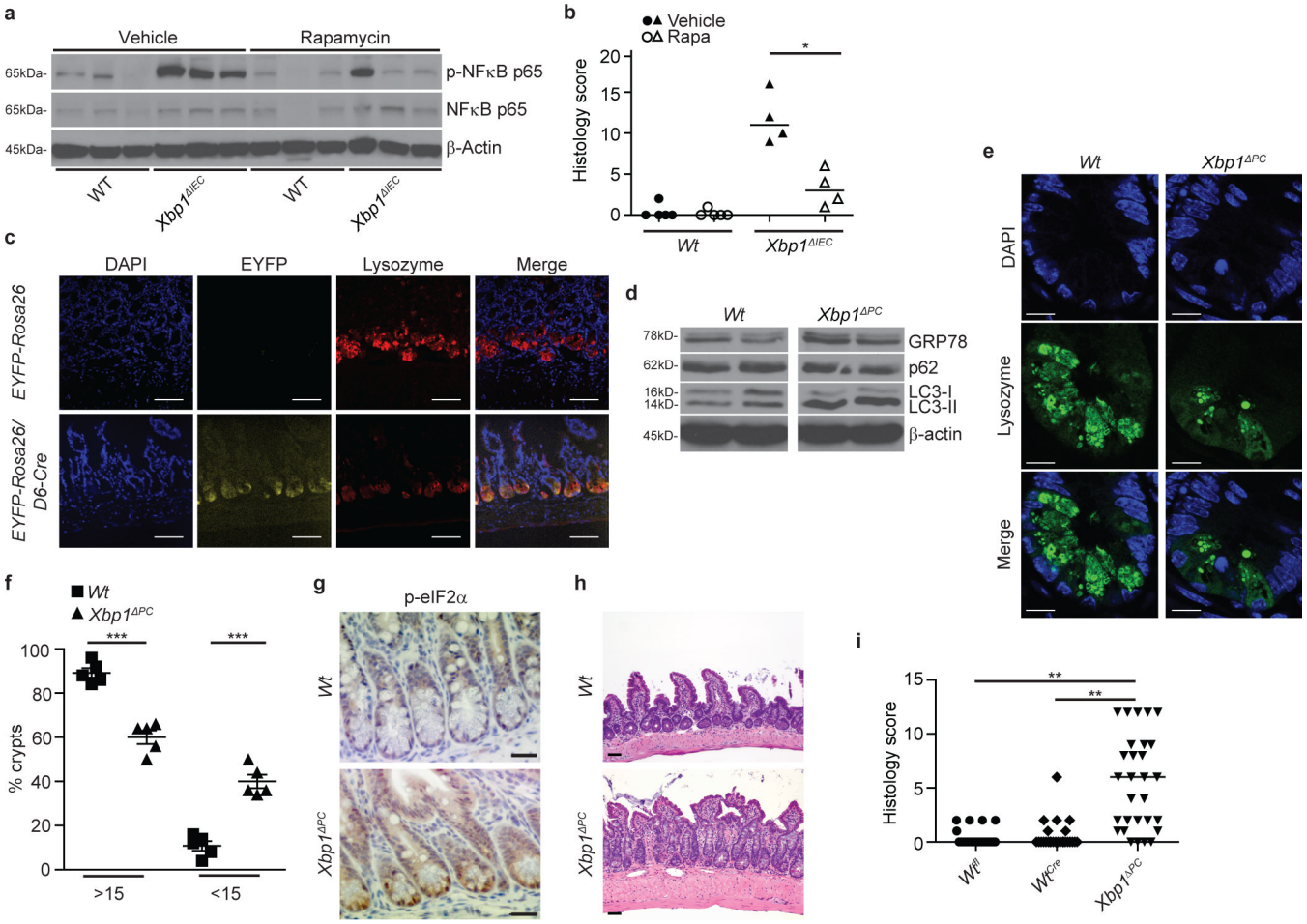

Figure 4. ER stress-induced enteritis originates from Paneth cells and is alleviated through autophagy induction

a, Immunoblot of primary IEC scrapings from mice treated with or without rapamycin for 14 consecutive days (n=3). **b,** Enteritis histology score for experiment as in (**a**) (n=4; median shown; Mann-Whitney U). **c,** Representative images of *EYFP-Rosa26/D6-Cre*$^{+/-}$ reporter mice and *EYFP-Rosa26* (controls). Co-localization of *Defa6* Cre-driven EYFP expression (yellow) with lysozyme expressing Paneth cells (red; n=3). DAPI, blue; bar, 50 μm. **d,** Immunoblots of crypt IECs from *Xbp1*$^{\Delta PC}$ and *Wt* controls (n=2). **e, f,** Representative confocal images of lysozyme (green) expressing Paneth cells (**e**) with quantification of crypts with indicated number of lysozyme^{+} granulated dots in (**f**) (n=5; unpaired Student's t-test). DAPI, blue; bar, 10 μm. **g,** Immunohistochemistry for p-eIF2α (n=3). Bar, 20 μm. **h,** Representative H&E images of *Xbp1*$^{\Delta PC}$ and *Wt* mice scored in (**i**). Bar, 50 μm. (**i**) Enteritis scoring in *Xbp1*$^{fl/fl}$ (*Wt*^{fl}), *Defa6 Cre*$^{+}$ (*Wt*^{Cre}) and *Defa6 Cre*$^{+}$;*Xbp1*$^{fl/fl}$ (*Xbp1*$^{\Delta PC}$) mice (n=21/26/29; median shown; Kruskal-Wallis with post-hoc Holm's-corrected Mann-Whitney U). Results represent two (**b, d**) independent experiments. *P < 0.05, **P < 0.01, ***P < 0.001.